Preparation of carbon nanosheets from petroleum asphalt via recyclable molten-salt method for superior lithium and sodium storage

Yixian Wang [a], Yuwei Wang [b], Jialiang Liu [a], Lei Pan [a], Wei Tian [a], Mingbo Wu [a, *], Jieshan Qiu [b, **]

[a] State Key Laboratory of Heavy Oil Processing, College of Chemical Engineering, China University of Petroleum, Qingdao 266580, China
[b] Carbon Research Laboratory, State Key Lab of Fine Chemicals, College of Chemical Engineering, Dalian University of Technology, Dalian 116024, China

ARTICLE INFO

ABSTRACT

Carbon nanosheets were successfully prepared from easily available and low-cost petroleum asphalt via a facile and recyclable molten-salt method. The as-made carbon nanosheets exhibit excellent performance on energy storage both for lithium-ion batteries (LIBs) and sodium-ion batteries (SIBs): as the anode of LIBs, they provide a high reversible specific capacity (729 mAh g^{-1} at 100 mA g^{-1}), excellent cyclability (600 mAh g^{-1} at 1 A g^{-1} after 500 cycles), and improved rate performance (280 mAh g^{-1} at 5 A g^{-1}). For SIBs, they also display a reversible capacity of 300 mAh g^{-1} at 50 mA g^{-1}, remarkable rate capability (90 mAh g^{-1} at 5 A g^{-1}) and retain as high as 95 mAh g^{-1} after 10000 cycles at 2 A g^{-1}. The superior electrochemical performance of carbon nanosheets could be attributed to their peculiar structural characteristics that integrate a variety of advantages: fast electronic and ionic conductivity, easy penetration of the electrolyte, shortened path for Li^+/Na^+ migration and structural stability. This approach paves the way for industrial scale-up due to its eco-friendliness, simplicity and versatility.

© 2017 Elsevier Ltd. All rights reserved.

1. Introduction

Lithium-ion batteries (LIBs), first commercialized by Sony in 1991, have been most widely used in the battery market of portable electronic devices, owing to their preeminent energy and power densities, enhanced safety and long-cycle lifespan [1—3]. Of late, the continuous progress and popularity of electric vehicles and hybrid electric vehicles have placed greater requirements on next-generation LIBs as far as larger energy density, longer lifetime, lower cost and more safety [4—6]. Graphite, the current state-of-the-art anode material in commercial LIBs, can hardly meet these demands because of its limited theoretical specific capacity (372 mAh g^{-1}) and rapid capacity fading [7]. Therefore, it is urgent to develop a better substitute for traditional graphite electrode. On the other hand, in consideration of the rarity and unevenly distribution of the lithium ore around the world, the price for further development of future large-scale energy storage system would

become a key issue [8]. To overcome these drawbacks, SIBs with greater abundance of sodium, much lower cost and similar working mechanism to LIBs, are regarded as one of the most promising alternatives to LIBs [9—11]. However, the progress on SIBs is relatively sluggish originating from the larger ionic radius of Na (1.06 Å) and heavier relative atomic mass (23 vs. Na) compared with those of its counterpart (0.76 Å and 6.94 vs. Li, respectively), which make them difficult to be reversibly inserted into and extracted from electrodes [12—14], for instance, the common graphite is electrochemically irreversible for SIBs [15]. In order to satisfy the surging need for electrical appliances and energy storage system, one feasible approach is to develop appropriate electrode materials with dual energy storage in both LIBs and SIBs.

Over the past few years, considerable contributions have been made in the structure design techniques of both cathode and anode materials for LIBs and SIBs [16—21]. In terms of anodes, carbonaceous materials such as carbon nanospheres, carbon nanotubes, graphene and their composites, have drawn tremendous attention on account of their natural availability, cost-effectiveness, good conductivity and nontoxicity [22—28]. Of these, two-dimensional (2D) carbon nanostructures, especially graphene and graphene-

* Corresponding author.
** Corresponding author.
E-mail addresses: wumb@upc.edu.cn (M. Wu), jqiu@dlut.edu.cn (J. Qiu).

like nanosheets, are being ever-increasing studied for energy storage equipment [29]. They benefit from the merits of high active surface area for sufficient electrolyte wetting, fast electrical conductivity through the electrodes, shortened path for charge carrier transportation and structural stability [30–32]. To this regard, various synthetic methods including mechanical/liquid-phase exfoliation [33], chemical vapor deposition [34], and template synthesis [35], have been put forward. Nevertheless, an overwhelming majority of the aforementioned means bear such drawbacks as time-consumption, high contamination and low yield, which seriously hinder their practicality and commercialization. Thus, it is of primary significance to open up a convenient, eco-friendly and sustainable route to fabricate 2D carbon materials.

Petroleum asphalt, as a major by-product of vacuum distillation of crude oil in petrochemical industry, has been mainly applied to low level utilization such as road pavement, water conservancy and roofing material in virtue of its viscoelastic and waterproof properties, which is a great waste of resources [5]. Taking account of the high carbon yield and aromaticity content of petroleum asphalt, it is imperative to take advantage of the readily available asphalt as carbon resources to manufacture high value-added carbon products. To this end, petroleum asphalt can be a good sort of raw materials to fabricate alternative carbonaceous anodes for batteries. Wei et al. prepared graphene from asphalt with the assistance of vermiculite template. The graphene anode exhibited high reversible capacities of 692 mAh g^{-1} at 50 mA g^{-1} and ~250 mAh g^{-1} at 1 A g^{-1} for LIBs [36]. Moreover, Song et al. synthesized mesophase-pitch derived mesoporous soft carbon utilizing nano-$CaCO_3$ template. The resultant carbon anode delivered superior sodium storage capacities of 331 mAh g^{-1} at 30 mA g^{-1} and 103 mAh g^{-1} at 500 mAh g^{-1} after 3000 cycles [37]. Although the above methods achieved high performance carbon materials from asphalt, the unrecyclable templates and hazardous chemicals used during the removal of these templates still incurred inevitable environmental cost to the final product.

Recently, Liu et al. demonstrated an interesting approach converting glucose to graphene through tuning carbonization conditions in a liquid molten-salt (MS) medium [38], which shed light on the possibility of assembling aromatic hydrocarbon into few-layer graphene sheets. Since petroleum asphalt contains a large amount of organic aromatic molecules, herein, petroleum asphalt was used as the raw material to prepare carbon nanosheets through a simple molten-salt method. A eutectic salt mixture of NaCl/KCl with a melting point of 657 °C was selected as the liquid media. The obtained carbon nanosheets were used as anode material both for LIBs and SIBs, their electrochemical performances and application possibilities were investigated.

2. Experimental

2.1. Samples synthesis

Petroleum asphalt (PA) obtained from Sinopec Group (7.1 wt% of saturates, 24.9 wt% of aromatics, 46.1 wt% of resins and 18.0 wt% of asphaltenes) was selected as the carbon precursor. All other chemicals were of analytical reagent grade and directly used without any further purification process. Typically, 0.5 g PA was dissolved in 20 ml toluene under sonication for 20 min. Then, 10 g eutectic composition of NaCl/KCl (4.5:5.5 by weight) were grounded in an agate mortar for 20 min and then added to the obtained solution. The above mixture was dried at 90 °C in an oil bath under mild magnetic stirring (160 rpm) to form a homogeneous mixture and reclaimed the toluene. The obtained dark-brown powder was thereafter transferred to a ceramic boat and put in the center of a tube furnace. Subsequently, the sample was heated to 800 °C at a ramp rate of 5 °C min^{-1} and dwelled for 2 h under a continuous nitrogen flow. After naturally cooled down to room temperature, the as-prepared sample was washed with sufficient deionized water to remove salts and collected by vacuum filtration, finally dried at 60 °C for 24 h to obtain the final sample nominated as MSC. For comparison, bare PA was treated by the same procedure without the addition of the eutectic salts and denoted as PAC.

For salt recycling test, after the sample was washed with deionized water, the resulting solution was collected by filtration, then heated at 90 °C to evaporate the water to obtain white crystals and finally dried at 100 °C overnight. The recovered salts were used to prepare the subsequent sample (denoted as RMSC) under the same condition.

2.2. Materials characterization

The morphologies of the as-prepared products were observed using field emission scanning electron microscopy (SEM, Hitachi S-4800). Transmission electron microscopy (TEM), selected area electron diffraction (SAED), and energy dispersive spectroscopy (EDS) were carried out on JEM-2010 system at 220 kV. X-ray diffraction (XRD, X'Pert PRO MPD) operated at 40 kV and 40 mA (Cu Kα radiation, λ = 1.5406 Å) and Raman spectroscopy (Renishaw RM2000) were used to examine the graphitization degree of the obtained samples. The interlayer spacing was calculated by Bragg equation (2dsinθ = nλ). The elemental composition and chemical bonding were studied by X-ray photoelectron spectroscopy (XPS, Thermo Scientific Escalab 250XI) with Mg Kα radiation and Fourier transform infrared spectra (FT-IR, Nicolet 6700 Spectrometer). Thermogravimetric analysis (TGA) was recorded on Shimadzu TA-60Ws Thermal Analyzer at a heating rate of 10 °C min^{-1}, from room temperature to 1000 °C in nitrogen. The pore property was tested by nitrogen adsorption-desorption isotherms on ASAP 2000 Micromeritics instrument.

2.3. Electrochemical measurements

The electrochemical performance was conducted with CR2032-type coin cells assembled in an argon-filled glove box (H_2O < 0.1 ppm, O_2 < 0.1 ppm). The working electrode was prepared by mixing 80 wt% as-prepared samples, 10 wt% carbon black, and 10 wt% poly(vinylidene fluoride) (PVDF) in N-methyl-2-pyrrolidinone (NMP) solvent to form a homogeneous slurry. Then the resulting slurry was pasted onto Cu foil, and dried in a vacuum oven at 80 °C for 12 h. The areal loading amount of the electrodes was about 0.8 mg cm^{-2}. LIBs were assembled with lithium metal foil as the counter electrode, 1 M $LiPF_6$ in a mixture of ethylene carbonate (EC)/dimethyl carbonate (DMC) (1:1 v/v) as the electrolyte, and polypropylene film as separators. For the assembly of SIBs, sodium metal foil served as the counter electrode, 1 M $NaClO_4$ in ethylene carbonate (EC)/diethyl carbonate (DEC) (1:1 v/v) was used as the electrolyte while the separator was made of glass fibers. The typical adding amount of the electrolyte in each cell was 80 μL for LIBs and 100 μL for SIBs. The galvanostatic charge-discharge tests were investigated by a Land CT2001A battery test system at a potential window of 0.01−3 V (vs. Li^+/Li) and 0.01−2.8 V (vs. Na^+/Na). Cyclic voltammetry (CV) at a scan rate of 0.1 mV s^{-1} and electrochemical impedance spectroscopy (EIS) at a frequency range of 100 kHz to 10 mHz with AC amplitude of 5 mV were both performed on CHI760D electrochemical workstation. All the electrochemical measurements were carried out at room temperature.

3. Results and discussion

The preparation procedures for MSC nanosheets are illustrated

in Fig. 1. First, the petroleum asphalt was uniformly mixed with the eutectic salts in toluene and a homogeneous mixture was obtained after the evaporation of the solvent. The mixture was then heated to approximately 400 °C where the carbonization of PAC took place while the salts remained solid. According to thermogravimetric analysis (TGA) in Fig. S1, the notable weight loss of PAC in this period was ascribed to the evaporation of volatile organic oil residues with smaller molecular weight [39]. When the annealing temperature elevated to 657 °C, the eutectic salts began to melt and form a liquid media. Subsequently, the system was shut down after keeping the mixture at 800 °C for 2 h. During the cooling process, the crystallization of molten salts pushed carbon out, therefore, carbon product and MS showed two separated phases [38]. Finally, the carbon nanosheets were easily obtained after the removal of MS by deionized water. It is worth noting that MSC retained a higher carbon yield of ~30 wt% compared with that of bare PAC (20.8 wt%), which is due to the existence of molten salts that act as barriers to buffer the escape of organic molecules. Meanwhile, the easily recovered molten salt could be reused to prepare subsequent carbon products, suggesting that the approach is sustainable and cost-effective.

Scanning electron microscopy (SEM) and transmission electron microscopy (TEM) techniques were used to uncover the morphologies and nanostructures of as-obtained samples. Fig. 2a reveals that MSC is predominantly constructed by interconnected lamellar architectures compared with the irregular bulk particles of PAC (Figs. S2a and S2b). Thin lamellas in Fig. 2b exhibit two-dimensional features and the thickness (red parallel lines) is below 20 nm, which is further proved by the corresponding TEM observation (Fig. 2c). In addition, Fig. S3 shows the thickness distribution of MSC with an average thickness of 13.8 nm. The "house of cards" structure of MSC provides sufficient active sites not only in the carbon layers but also in the voids between different nanosheets [40]. Furthermore, the sheet-like structure furnishes a shortened diffusion path of ions in the thickness direction and easy electron transport pathways through its carbon network [41]. According to HRTEM images in Fig. 2d and Fig. S2c, MSC is poorly crystallized and contains small domains of contacted graphite micro-crystallites (highlighted by the red boxes), while the margin of PAC is constructed by successive paralleled graphene nanosheets (highlighted by red arrows), indicating a higher graphitization degree. The lattice spacing of MSC is around 0.36 nm and larger

than that of PAC (0.34 nm), which indicates the enlarged carbon interlayer distance, thereby accelerating the migration of ions [42]. The faint dispersing diffraction ring in selected area electron diffraction (SAED) patterns verifies the amorphous structure of MSC [43,44]. The energy dispersive spectroscopy (EDS) elemental mapping results (Fig. 2e−g) evidently demonstrate the homogeneous distribution of C and O. Clearly, the existence of MS makes a big difference to morphology transformation from bulk PAC to 2D nanosheets MSC. The resulting amorphous structure and expanded lattice distance are of great benefit to Li^+/Na^+ storage.

X-ray diffraction (XRD) profiles for PAC and MSC samples are shown in Fig. 3a. As can be seen, both of them display two peaks at approximately 26° and 42°, which are related to the (002) and (100) planes of typical amorphous carbon, respectively. The broader and weaker diffraction peaks of MSC indicate a more disordered structure compared with PAC. The interlayer spacing (d_{002}) of MSC is calculated to be ~0.358 nm, which is in good agreement with TEM result, and larger than ~0.348 nm of PAC and significantly wider than 0.335 nm of graphite. Particularly, the large vacant space between graphene layers is reported to facilitate the reversible storage of sodium considering the larger radius of Na^+ (1.06 Å) than that of Li^+ (0.76 Å) [45].

The graphitization degrees of PAC and MSC were further characterized by Raman spectroscopy. In the Raman spectra (Fig. 3b), two peaks around 1356 cm^{-1} (D band) and 1596 cm^{-1} (G band) can be distinguished, respectively. The D band corresponds to edge planes and structure defects of graphite crystals, while the G band is associated with the vibration of sp^2-bonded graphitic carbon atoms [46]. The peak intensity ratio of MSC ($I_D/I_G = 0.89$) is higher than that of PAC ($I_D/I_G = 0.81$), confirming the higher disordered degree with abundant defects because of the structural distortion induced by MS, which is in accordance with TEM and XRD characterization.

Brunauer-Emmett-Teller (BET) measurement was used to examine the pore structures of the samples. As shown in Fig. 3c, MSC exhibits a type IV adsorption-desorption isotherm with a BET specific surface area (SSA) of 11 m^2 g^{-1}, while PAC only has a SSA of 4 m^2 g^{-1}, suggesting a slight increase of porosity introduced by MS system. The pore-size distribution demonstrates the micro-mesoporous structure of MSC with an average micropore width of 0.86 nm (Horvath-Kawazoe method) and mesopore width of 14.6 nm (BJH method). The hierarchical pores of the MSC
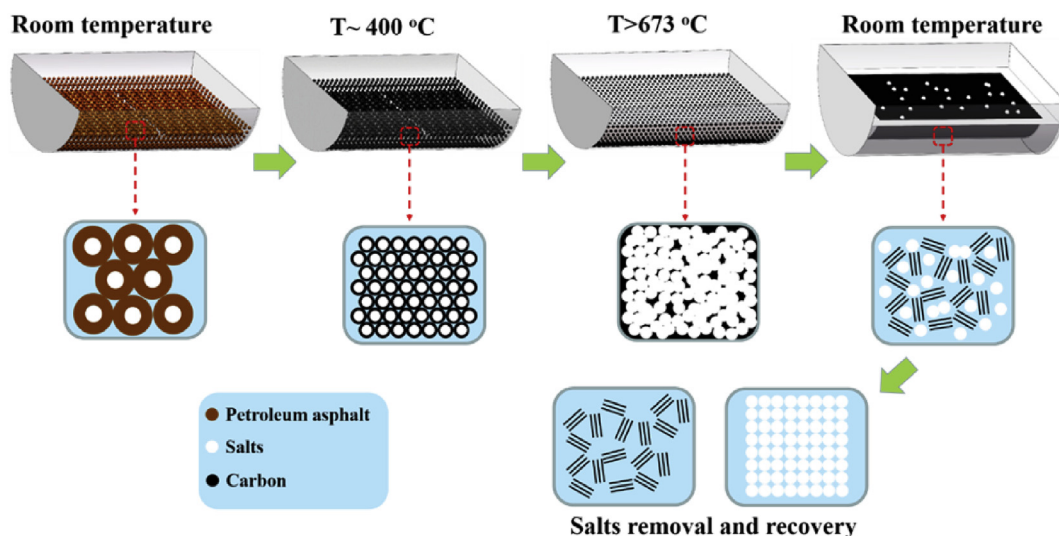

Fig. 1. Schematic illustration of the preparation process for the carbon nanosheets in Molten-salt system. (A colour version of this figure can be viewed online.)
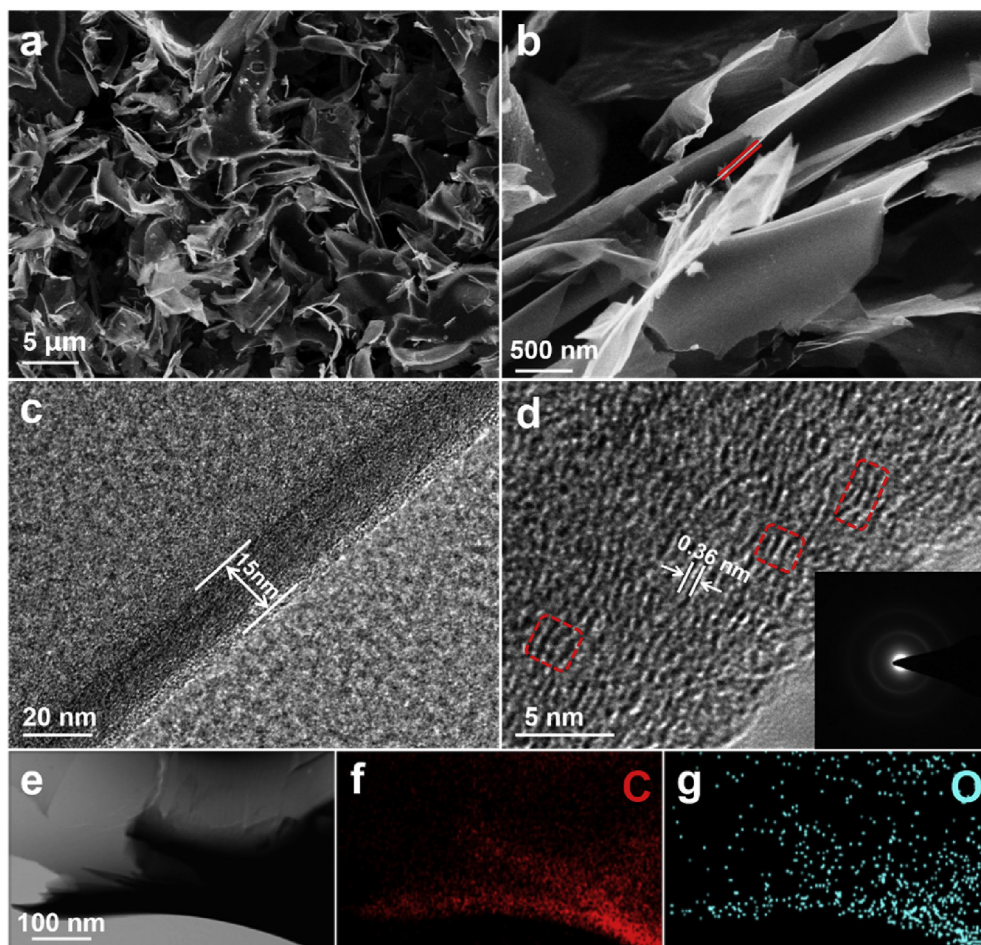
Fig. 2. (a, b) SEM images, (c) TEM and (d) HRTEM images of MSC. (e, f, g) EDS elemental mapping of MSC. (A colour version of this figure can be viewed online.)

necessarily not only ensure the sufficient electrode/electrolyte interface and fast ionic transportation, but also act as "reservoirs" for Li$^+$/Na$^+$ storage.

The nature and types of chemical groups in MSC sample were examined by X-ray photoelectron spectroscopy (XPS), and the XPS survey spectrum is shown in Fig. S4a with two pronounced peaks at 284.6 eV (C1s) and 532.6 eV (O1s). The much weaker of O1s peak implies only a few oxygen-containing groups exist, verified by 3.7 at.% of oxygen compared with 96.3 at.% of carbon. Fig. 3d illustrates the high-resolution of C1s XPS spectrum, peaks at 284.6, 285.9 and 288.8 eV are ascribed to C=C/C–C, C–O and C=O functional groups, respectively [47]. The high-resolution spectrum of O1s in Fig. S4b evidences the existence of oxygen-containing groups, i.e. C–O–C, C=O and C–OH. The elemental composition of MSC is summarized in Table S1. Besides, in order to further study the chemical states of oxygen in MSC, Fourier transform infrared (FT-IR) spectroscopy and was performed. As shown in Fig. S5, the peaks of C–OH (3430 cm^{-1}), C=O (~1700 cm^{-1}) and C–O (~1100 cm^{-1}) could be corroborated by FT-IR spectrum [38,48]. It is reported that these oxygen-containing groups could enhance lithium and sodium storage by increasing interlayer distance between graphene layers [49]. Nevertheless, these functional groups would partially react with the electrolyte, eventually resulting in low Coulombic efficiency [17].

In order to evaluate the electrochemical performance of the as-made samples for both LIBs and SIBs, PAC and MSC were coated onto Cu foil as anodes with Li or Na metal foil as counter and

reference electrode to assemble CR2032-type half cells. Fig. 4a and b shows the first three consecutive cyclic voltammetry (CV) plots of MSC at a scan rate of 0.1 mV s^{-1}, which are obtained within the voltage range of 0.01–3 V (vs. Li$^+$/Li) and 0.01–2.8 V (vs. Na$^+$/Na). In general, the MSC anode displays typical CV curves of carbon-based materials in previous reports [47,50]. For LIBs, the sharp cathodic peak at 0.01 V and two broad anodic peaks at 0.2 V and ~1.1 V are attributed to the reversible insertion/extraction of Li$^+$ into/from the graphitic nanosheets and the nanocavities [51]. As such, the insertion/extraction processes of Na$^+$ into/from carbon layers and nanovoids generate a pronounced pair of redox peaks at 0.01–0.1 V in SIBs [25]. In addition, a pair of small and broad redox peaks can be observed at 0.3–1.0 V, corresponding to the charge transfer on the surface of small graphitic clusters [52]. The two noticeable cathodic peaks at around 0.8 V and 0.35 V in LIBs, 1 V and 0.45 V in SIBs during the first discharge cycle result from the reaction between Li/Na with functional groups on the carbon surface and the formation of a solid electrolyte interphase (SEI), respectively [53,54]. However, these peaks vanish in the following circles, indicating that the reactions to form SEI film are irreversible. Besides, subsequent curves show good repeatabilities with negligible changes, implying an outstanding cycling performance of the MSC.

Fig. 4c describes the galvanostatic charge/discharge curves of MSC for LIBs at a current of 100 mA g^{-1} in a potential range 0.01–3 V (vs. Li$^+$/Li). An initial capacity of 1353 mAh g^{-1} is obtained from the first delithiation, while the first lithiation gives a reversible capacity of 729 mAh g^{-1}, leading to an initial Coulombic
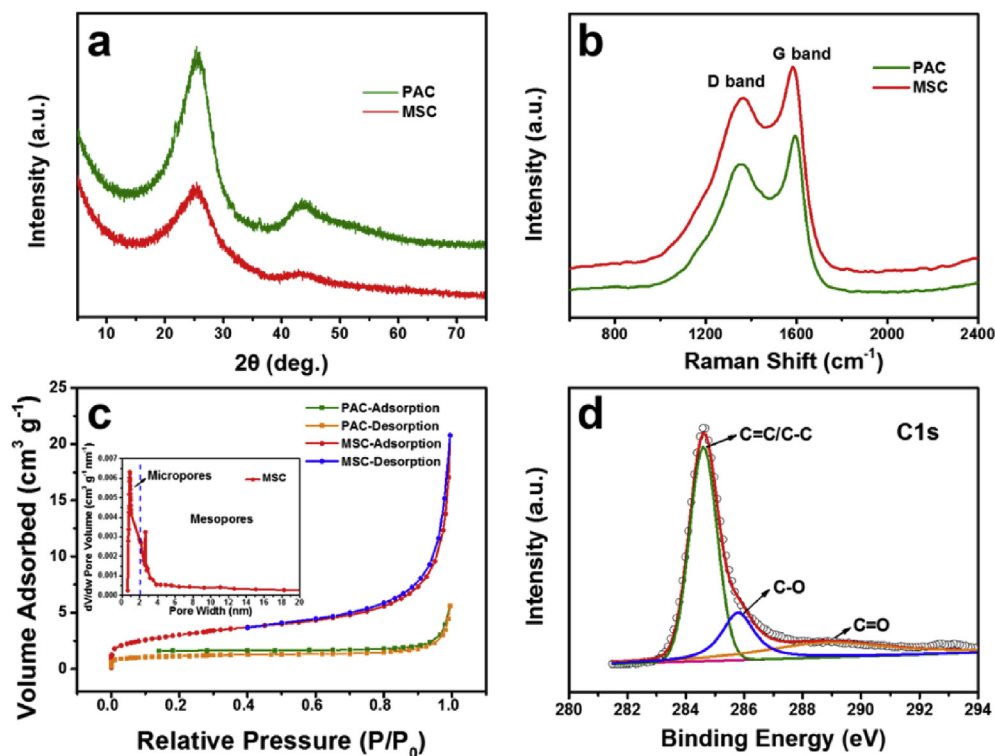
Fig. 3. (a) XRD patterns, (b) Raman spectra and (c) Nitrogen adsorption-desorption isotherms of PAC and MSC with pore-size distribution (inset). (d) XPS high-resolution of C1s spectrum of MSC. (A colour version of this figure can be viewed online.)
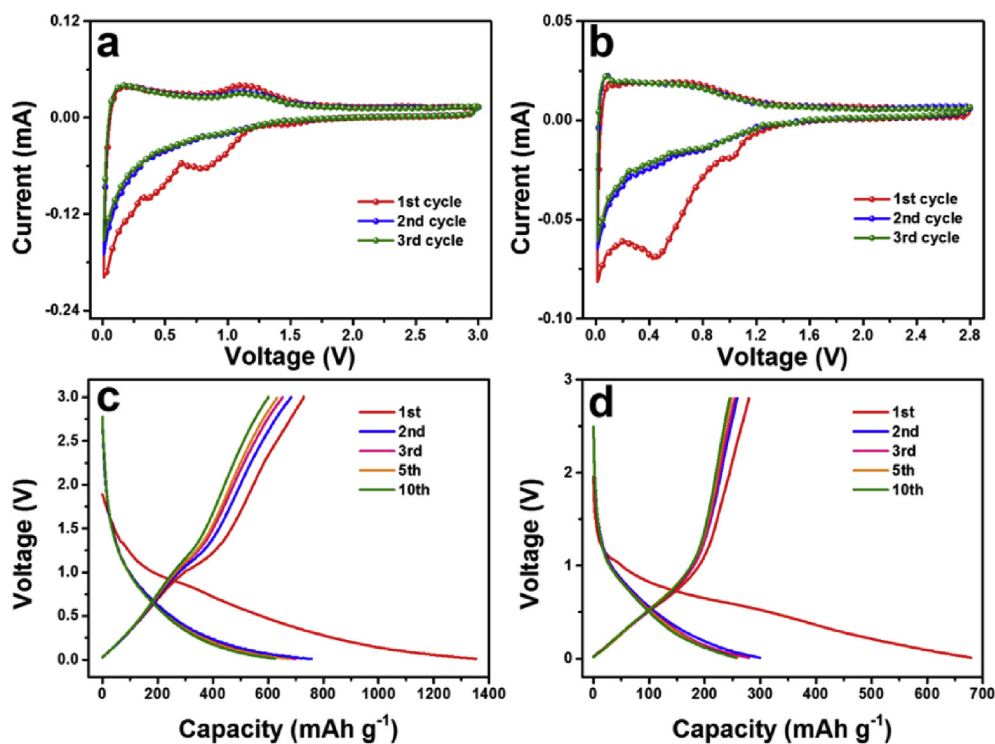

Fig. 4. CV curves of MSC at a scan rate of 0.1 mV s^{-1} for (a) LIBs and (b) SIBs. Galvanostatic charge and discharge profiles of MSC electrode for (c) LIBs cycled between 0.01 and 3 V (vs. Li$^+$/Li) at the current density of 100 mA g^{-1} and (d) SIBs cycled between 0.01 and 2.8 V (vs. Na$^+$/Na) at the current density of 50 mA g^{-1}. (A colour version of this figure can be viewed online.)

efficiency (CE) of 53.9%. The irreversible capacity is mainly caused by the consumption of Li$^+$ during the formation of SEI film, which is

consistent with CV plots. As is seen from Fig. 4d, the charge/discharge profiles for SIBs resemble those of LIBs except for a lower

capacity as a result of a larger Na$^+$ radius than Li$^+$. The MSC electrode delivers initial discharge/charge capacities of 679 and 279 mAh g^{-1}, when tested at a current density of 50 mA g^{-1} between 0.01 and 2.8 V (vs. Na$^+$/Na). The low initial CE of MSC in SIBs (~41%) is also correlated to the formation of SEI layer. After the obvious capacity loss in the first cycle, the CE of MSC for both LIBs and SIBs rapidly improve to near 100%, reflecting high reversibility both for lithium and sodium storage.

In Fig. 5a, the cyclic performances of the as-made samples for LIBs were investigated at the current density of 1 A g^{-1} for 500 cycles. To fully activate the electrode, 100 mA g^{-1} was applied in the first five cycles. After that, the MSC electrode exhibits a higher reversible capacity of 382 mAh g^{-1} compared with PAC (270 mAh g^{-1}) at the beginning. However, the cycling curve of MSC presents two distinctive stages afterwards. In the first stage, the capacity undergoes a slow drop to 340 mAh g^{-1} after 40 cycles while the second stage witnesses a gradual growth of the reversible capacity up to 607 mAh g^{-1} at the end of 410th cycle, and then it experiences small ups and downs around 600 mAh g^{-1} till 500

cycles. One possible reason for the activation of the anode material is due to the partially crystallinity degradation of the graphitized carbon to a more disordered degree, exposing more active sites for lithium storage between interconnected nanosheets upon deep cycling and leading to better contact of the electrode with the electrolyte [21,55]. By contrast, the PAC electrode delivers lower starting capacity and suffers a drastic capacity decrease after 300 cycles because of the structural deterioration so that only 155 mAh g^{-1} is maintained in the end. The cycling stabilities of PAC and MSC in SIBs were measured at 1 A g^{-1} for 500 cycles including the activation process. As shown in Fig. 5b, MSC delivers much higher initial discharge capacity of 730 mAh g^{-1} at 100 mAh g^{-1} and a slightly lower initial CE (33%) (381 mAh g^{-1} and 41%, respectively). Meanwhile, the reversible capacity of MSC is retained at 108 mAh g^{-1} at 2 A g^{-1} after 500 cycles, in stark contrast to that of PAC (44 mAh g^{-1}). More impressively, after ultra-long 10000 cycles at 2 A g^{-1} (Fig. 5c), a reversible capacity of 95 mAh g^{-1} for MSC anode can still be recovered with a low average capacity decay rate of ~0.1% per cycle. The extraordinary cycling performance of
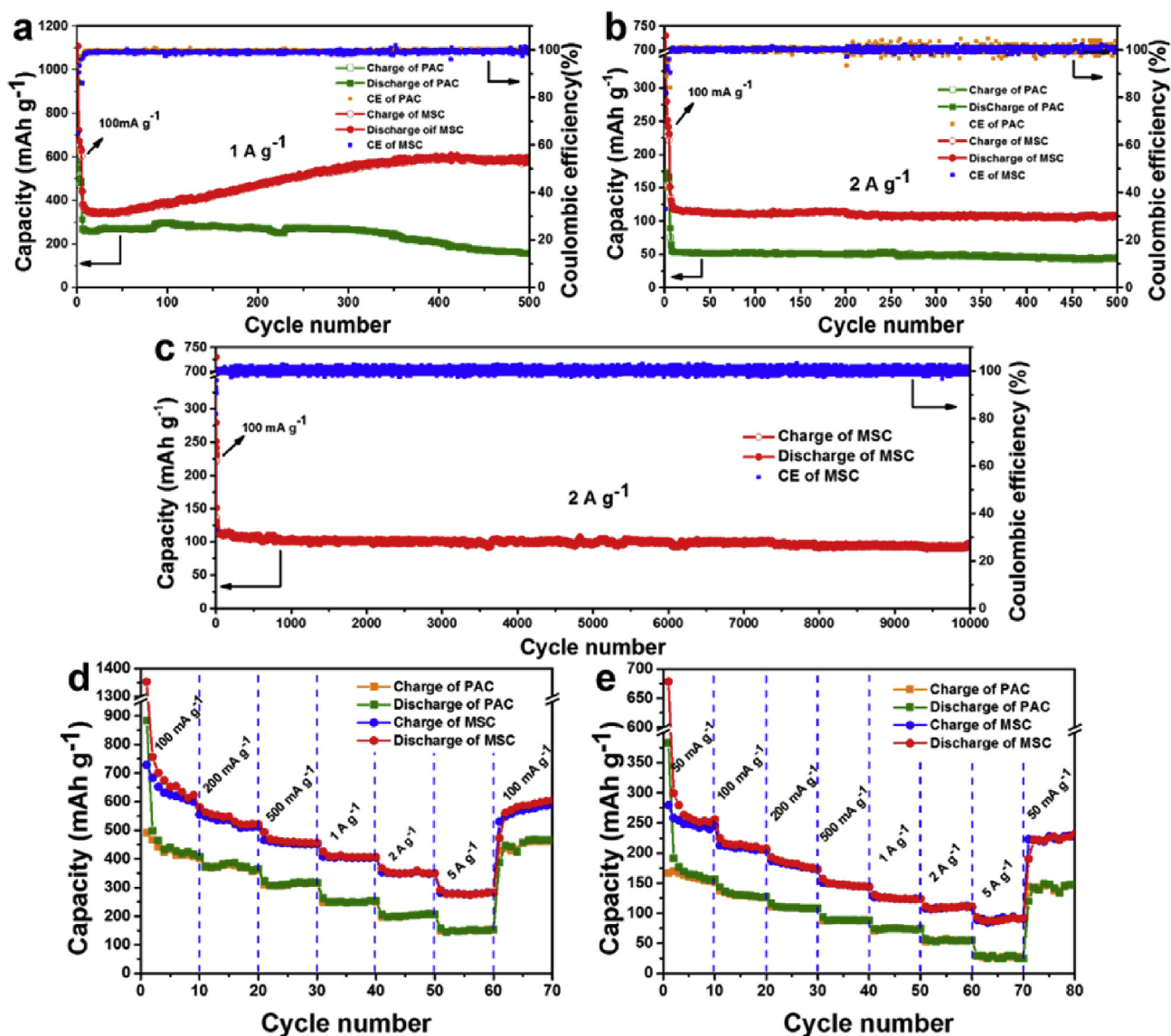

Fig. 5. Cycling performances of PAC and MSC at a cycling rate of 1 A g^{-1} for LIBs (a) and 2 A g^{-1} for SIBs (b) (100 mA g^{-1} was used for activation at first 5 cycles). (c) Ultra-long cycling performance of MSC at the current density of 2 A g^{-1} for SIBs. (d) and (e) Rate performances of PAC and MSC. (A colour version of this figure can be viewed online.)

the MSC anode for SIBs relies on the ultra-stable skeleton of the carbon nanosheets, which can buffer the mechanical stress during sodiation and desodiation. Moreover, the long-term durability holds strong potential for practical application.

Remarkably, both LIBs and SIBs can recover high capacity retention when abruptly switching to lower current density, implying the structure integrity of the MSC anode during the Li^+/Na^+ insertion and extraction without obvious degradation or pulverization under high-rate test. It is worth mentioning that the outstanding reversibility for Li/Na storage of MSC can be seen from the well overlaps of discharge and charge capacities with high CE approaching 100% even at 5 A g^{-1}. To the best of our knowledge, such prominent electrochemical performance of carbonaceous materials both for LIBs and SIBs based on cycling stability and rate capability has seldom been fulfilled in previous reports (Tables S2 and S3). Additionally, the delicate 2D-nanosheets are favorable to electronic conductivity and ionic transport, which can be further validated by the electrochemical impedance spectroscopy (EIS) in Fig. S6. The high frequency semicircles (amplified in the insets) of the MSC in LIBs and SIBs before and after 50 cycles remain smaller value, suggesting lower charge transfer resistance compared with those of PAC. Besides, the low frequency slope angles for MSC are steeper than those for PAC, standing for faster Li/Na ions diffusion in MSC electrode [56].

In order to study the recyclability of the molten salts, a sequence of measurements was done afterwards. As depicted in Fig. S7a, the recycled MS kept white crystals with a little weight loss ~4%, which was mainly owing to the transfer process and slight evaporation during calcination. Meanwhile, the components of recycled MS were detected to be unchanged comprising of pure NaCl and KCl. Such results manifest the eutectic MS is recyclable after a simple filtration and drying process. Furthermore, RMSC was prepared using recycled MS and its XRD pattern (Fig. S7b) is similar to that of MSC, demonstrating the disordered structure without any impurity. Figs. S8a and S8b present the electrochemical capabilities of the RMSC anode, it exhibits reversible capacities of 601 mAh g^{-1} after 500 cycles at the current density of 1 A g^{-1} for LIBs and 96 mAh g^{-1} after 5000 cycles at 2 A g^{-1} for SIBs, respectively. The outstanding cycling performance of RMSC is comparable to MSC, which certifies the fully recyclable feather of MS.

The above results evidently manifest that the distinct characters of MSC are responsible for its high reversible capacity, enduring cycling stability and outstanding rate capability as an anode for both LIBs and SIBs, which can be summarized as follows. First, the "house of cards" structure can provide substantial defects and abundant active sites for Li^+/Na^+ storage. Second, the expanded graphitic interlayer spacing and enlarged surface area not only promote the electrolyte mass-transfer in the voids, but also lead to a shortened path and lessened barrier for Li^+/Na^+ insertion/extraction, thus achieving rapid ion diffusion. Third, the interconnected 2D-nanosheets would facilitate fast charge transport as well as easy penetration of the electrolyte. Moreover, the standout structural robustness of MSC can markedly alleviate the volume change of the carbon anode material, hence contributing to the brilliant cycling performance.

4. Conclusion

In summary, we report a facile and recyclable strategy to fabricate disordered carbon nanosheets through the carbonization of petroleum asphalt in molten salts. The amorphous carbon with enlarged interlayer space and abundant defects is in favor of Li^+/Na^+ storage and transport while the two-dimensional nanosheets ensure the intimate contact with electrolyte, promoted electrode interaction with the conductive network and structural integrity.

When served as the anode material for LIBs and SIBs, the robust carbon skeleton renders the electrode superior electrochemical performances. Consequently, the carbon nanosheets exhibit a high reversible specific capacity (729 mAh g^{-1} at 100 mA g^{-1}), outstanding cyclability (600 mAh g^{-1} at 1 A g^{-1} after 500 cycles), and improved rate performance (280 mAh g^{-1} at 5A g^{-1}) for LIBs. As anode for SIBs, they also deliver a high sodium storage capacity (300 mAh g^{-1} at 50 mA g^{-1}), remarkable rate capability (90 mAh g^{-1} at 5 A g^{-1}) and long-term cycle stability (95 mAh g^{-1} at 2 A g^{-1} after 10000 cycles). More importantly, this work opens up a new avenue for low-cost, scalable, and sustainable synthesis of promising anodes for rechargeable Li/Na ion batteries.

Acknowledgments

Appendix A. Supplementary data

Supplementary data related to this article can be found at http://dx.doi.org/10.1016/j.carbon.2017.06.086.

References

[1] M. Armand, J.M. Tarascon, Building better batteries, Nature 451 (2008) 652–657.
[2] J.B. Goodenough, K.S. Park, The Li-ion rechargeable battery: a perspective, J. Am. Chem. Soc. 135 (2013) 1167–1176.
[3] K. Kang, Y.S. Meng, J. Bréger, C.P. Grey, G. Ceder, Electrodes with high power and high capacity for rechargeable lithium batteries, Science 311 (2006) 977–980.
[4] F. Sun, J. Gao, H. Wu, X. Liu, L. Wang, X. Pi, et al., Confined growth of small ZnO nanoparticles in a nitrogen-rich carbon framework: advanced anodes for long-life Li-ion batteries, Carbon 113 (2017) 46–54.
[5] P. Li, J.Y. Liu, Y. Liu, Y.W. Wang, Z.T. Li, W.T. Wu, et al., Three-dimensional ZnMn2O4/porous carbon framework from petroleum asphalt for high performance lithium-ion battery, Electrochim. Acta 180 (2015) 164–172.
[6] J.K. Ou, L. Yang, Z. Zhang, X.H. Xi, Honeysuckle-derived hierarchical porous nitrogen, sulfur, dual-doped carbon for ultra-high rate lithium ion battery anodes, J. Power Sources 333 (2016) 193–202.
[7] X.H. Li, Y.B. He, C. Miao, X.Y. Qin, W. Lv, H.D. Du, et al., Carbon coated porous tin peroxide/carbon composite electrode for lithium-ion batteries with excellent electrochemical properties, Carbon 81 (2015) 739–747.
[8] G. Lee, M.R. Jo, K. Zhang, Y. Kang, A reduced graphene oxide-encapsulated phosphorus/carbon composite as a promising anode material for high-performance sodium-ion batteries, J. Mater. Chem. A 5 (2017) 3683–3690.
[9] M.D. Slater, D. Kim, E. Lee, C.S. Johnson, Sodium-ion batteries, Adv. Funct. Mater 23 (2013) 947–958.
[10] C. Chen, Y. Wen, X. Hu, X. Ji, M. Yan, L. Mai, et al., Na(+) intercalation pseudocapacitance in graphene-coupled titanium oxide enabling ultra-fast sodium storage and long-term cycling, Nat. Commun. 6 (2015) 6929.
[11] J. Yang, X. Zhou, D. Wu, X. Zhao, Z. Zhou, S-doped N-Rich carbon nanosheets with expanded interlayer distance as anode materials for sodium-ion batteries, Adv. Mater 29 (2017) 1604108.
[12] N. Yabuuchi, K. Kubota, M. Dahbi, S. Komaba, Research development on sodium-ion batteries, Chem. Rev. 114 (2014) 11636–11682.
[13] H. Kim, H. Kim, Z. Ding, M.H. Lee, K. Lim, G. Yoon, et al., Recent progress in electrode materials for sodium-ion batteries, Adv. Energy Mater 6 (2016) 1600943.
[14] S.W. Zhang, W. Lv, C. Luo, C.H. You, J. Zhang, Z.Z. Pan, et al., Commercial carbon molecular sieves as a high performance anode for sodium-ion batteries, Energy Storage Mater 3 (2016) 18–23.
[15] P. Ge, M. Fouletier, Electrochemical intercalation of sodium in graphite, Solid State Ion. 28 (1988) 1172–1175.
[16] Y. Sun, N. Liu, Y. Cui, Promises and challenges of nanomaterials for lithium-based rechargeable batteries, Nat. Energy 1 (2016) 16071.
[17] L.H. Yin, Y.X. Wang, C.C. Han, Y.M. Kang, X. Ma, H. Xie, et al., Self-assembly of disordered hard carbon/graphene hybrid for sodium-ion batteries, J. Power Sources 305 (2016) 156–160.
[18] W. Li, Z. Yang, M. Li, Y. Jiang, X. Wei, X. Zhong, et al., Amorphous red phosphorus embedded in highly ordered mesoporous carbon with superior lithium and sodium storage capacity, Nano Lett. 3 (2016) 1546–1553.
[19] F. Zou, Y.M. Chen, K. Liu, Z. Yu, W. Liang, S.M. Bhaway, et al., Metal organic

frameworks derived hierarchical hollow NiO/Ni/graphene composites for lithium and sodium storage, ACS Nano 10 (2016) 377–386.

[20] L. Yu, H.B. Wu, X.W. Lou, Self-templated formation of hollow structures for electrochemical energy applications, Acc. Chem. Res. 50 (2017) 293–301.

[21] S. Zhang, F. Yao, L. Yang, F. Zhang, S. Xu, Sulfur-doped mesoporous carbon from surfactant-intercalated layered double hydroxide precursor as high-performance anode nanomaterials for both Li-ion and Na-ion batteries, Carbon 93 (2015) 143–150.

[22] X.Y. Yue, W. Sun, J. Zhang, F. Wang, Y.X. Yang, C.Y. Lu, et al., Macro-meso-porous hollow carbon spheres as anodes for lithium-ion batteries with high rate capability and excellent cycling performance, J. Power Sources 331 (2016) 10–15.

[23] M. Mao, J.Y. Hu, H.T. Liu, Graphene-based materials for flexible electro-chemical energy storage, Int. J. Energy Res. 39 (2015) 727–740.

[24] H.Y. Chen, N. Bucher, S. Hartung, L.L. Li, J. Friedl, H.P. Liou, et al., A multi-walled carbon nanotube core with graphene oxide nanoribbon shell as anode material for sodium ion batteries, Adv. Mater. Interfaces 3 (2016) 1600357.

[25] M. Wang, Z. Yang, W. Li, L. Gu, Y. Yu, Superior sodium storage in 3D inter-connected nitrogen and oxygen dual-doped carbon network, Small 19 (2016) 2559–2566.

[26] J.F. Cui, Y.L. Xi, S. Chen, D.H. Li, X.L. She, J. Sun, et al., Prolifera-green-tide as sustainable source for carbonaceous aerogels with hierarchical pore to achieve multiple energy storage, Adv. Funct. Mater 26 (2016) 8487–8495.

[27] M.-S. Balogun, Y. Luo, W. Qiu, P. Liu, Y. Tong, A review of carbon materials and their composites with alloy metals for sodium ion battery anodes, Carbon 98 (2016) 162–178.

[28] X.B. Cheng, G.L. Tian, X.F. Liu, J.Q. Nie, M.Q. Zhao, J.Q. Huang, et al., Robust growth of herringbone carbon nanofibers on layered double hydroxide derived catalysts and their applications as anodes for Li-ion batteries, Carbon 62 (2013) 393–404.

[29] D. Yoon, D.H. Kim, K.Y. Chung, W. Chang, S.M. Kim, J. Kim, Hydrogen-enriched porous carbon nanosheets with high sodium storage capacity, Carbon 98 (2016) 213–220.

[30] L. Peng, Y. Zhu, D. Chen, R.S. Ruoff, G. Yu, Two-dimensional materials for beyond-lithium-ion batteries, Adv. Energy Mater 6 (2016) 1600025.

[31] H.G. Wang, Z. Wu, F.L. Meng, D.L. Ma, X.L. Huang, L.M. Wang, et al., Nitrogen-doped porous carbon nanosheets as low-cost, high-performance anode material for sodium-ion batteries, ChemSusChem 6 (2013) 56–60.

[32] R. Raccichini, A. Varzi, D. Wei, S. Passerini, Critical insight into the relentless progression toward graphene and graphene-containing materials for lithium-ion battery anodes, Adv. Mater 29 (2016) 1603421.

[33] V. Nicolosi, M. Chhowalla, M.G. Kanatzidis, M.S. Strano, J.N. Coleman, Liquid exfoliation of layered materials, Science 340 (2013) 1226419.

[34] S. Park, R.S. Ruoff, Chemical methods for the production of graphenes, Nat. Nanotechnol. 5 (2010) 309–309.

[35] X.M. Fan, C. Yu, J. Yang, Z. Ling, C. Hu, M.D. Zhang, et al., A layered-nanospace-confinement strategy for the synthesis of two-dimensional porous carbon nanosheets for high-rate performance supercapacitors, Adv. Energy Mater 5 (2015) 1401761.

[36] C.G. Xu, G.Q. Ning, X. Zhu, G. Wang, X.F. Liu, J.S. Gao, et al., Synthesis of graphene from asphaltene molecules adsorbed on vermiculite layers, Carbon 62 (2013) 213–221.

[37] B. Cao, H. Liu, B. Xu, Y.F. Lei, X.H. Chen, H.H. Song, Mesoporous soft carbon as an anode material for sodium ion batteries with superior rate and cycling performance, J. Mater. Chem. A 4 (2016) 6472–6478.

[38] X. Liu, C. Giordano, M. Antonietti, A facile molten-salt route to graphene synthesis, Small 10 (2014) 193–200.

[39] A.S. Jalilov, Y. Li, J. Tian, J.M. Tour, Ultra-high surface area activated porous asphalt for CO_2 capture through competitive adsorption at high pressures, Adv. Energy Mater 7 (2016) 1600693.

[40] Z. Guo, C. Wang, M. Chen, M. Li, Hard carbon derived from coal tar pitch for use as the anode material in lithium ion batteries, Int. J. Electrochem. Sci. 8 (2013) 2702–2709.

[41] S.H. Yu, D.J. Lee, M. Park, S.G. Kwon, H.S. Lee, A. Jin, et al., Hybrid cellular nanosheets for high-performance lithium-ion battery anodes, J. Am. Chem. Soc. 137 (2015) 11954–11961.

[42] X.B. Cheng, Q. Zhang, H.F. Wang, G.L. Tian, J.Q. Huang, H.J. Peng, et al., Nitrogen-doped herringbone carbon nanofibers with large lattice spacings and abundant edges: catalytic growth and their applications in lithium ion batteries and oxygen reduction reactions, Catal. Today 249 (2015) 244–251.

[43] Y.M. Li, Y.S. Hu, H. Li, L.Q. Chen, X.J. Huang, A superior low-cost amorphous carbon anode made from pitch and lignin for sodium-ion batteries, J. Mater. Chem. A 4 (2016) 96–104.

[44] Z. Tan, K. Ni, G. Chen, W. Zeng, Z. Tao, M. Ikram, et al., Incorporating pyrrolic and pyridinic nitrogen into a porous carbon made from C60 molecules to obtain superior energy storage, Adv. Mater 29 (2017) 1603414.

[45] X.S. Zhou, Y.G. Guo, Highly disordered carbon as a superior anode material for room-temperature sodium-ion batteries, ChemElectroChem 1 (2014) 83–86.

[46] Y. Wang, D.C. Alsmeyer, R.L. Mccreery, Raman spectroscopy of carbon materials: structural basis of observed spectra, Chem. Mater 2 (1990) 557–563.

[47] Y. Liu, L. Fan, L. Jiao, Graphene highly scattered in porous carbon nanofibers: a binder-free and high-performance anode for sodium-ion batteries, J. Mater. Chem. A 5 (2017) 1698–1705.

[48] L. Fan, B. Lu, Reactive oxygen-doped 3D interdigital carbonaceous materials for Li and Na ion batteries, Small 12 (2016) 2783–2791.

[49] Y. Wen, K. He, Y. Zhu, F. Han, Y. Xu, I. Matsuda, et al., Expanded graphite as superior anode for sodium-ion batteries, Nat. Commun. 5 (2014) 4033.

[50] K. Tang, R.J. White, X. Mu, M.M. Titirici, P.A. van Aken, J. Maier, Hollow carbon nanospheres with a high rate capability for lithium-based batteries, ChemSusChem 5 (2012) 400–403.

[51] P. Li, J.Y. Liu, Y.W. Wang, Y. Liu, X.N. Wang, K.W. Nam, et al., Synthesis of ultrathin hollow carbon shell from petroleum asphalt for high-performance anode material in lithium-ion batteries, Chem. Eng. J. 286 (2016) 632–639.

[52] Y. Cao, L. Xiao, M.L. Sushko, W. Wang, B. Schwenzer, J. Xiao, et al., Sodium ion insertion in hollow carbon nanowires for battery applications, Nano Lett. 12 (2012) 3783–3787.

[53] M. Chen, C. Yu, S. Liu, X. Fan, C. Zhao, X. Zhang, et al., Micro-sized porous carbon spheres with ultra-high rate capability for lithium storage, Nanoscale 7 (2015) 1791–1795.

[54] Y.M. Li, Y.S. Hu, M.M. Titirici, L.Q. Chen, X.J. Huang, Hard carbon microtubes made from renewable cotton as high-performance anode material for sodium-ion batteries, adv, Energy Mater 6 (2016) 1600659.

[55] S.S. Niu, Z.Y. Wang, T. Zhou, M.L. Yu, M.Z. Yu, J.S. Qiu, A polymetallic metal-organic framework-derived strategy toward synergistically multidoped metal oxide electrodes with ultralong cycle life and high volumetric capacity, Adv. Funct. Mater 27 (2017) 1605332.

[56] C. Zhang, X. Wang, Q. Liang, X. Liu, Q. Weng, J. Liu, et al., Amorphous phosphorus/nitrogen-doped graphene paper for ultrastable sodium-ion batteries, Nano Lett. 16 (2016) 2054–2060.